Phase identification and discovery of hidden crystal forms in a polycrystalline pharmaceutical sample using high-throughput 3D electron diffraction

Molly Lightowler[a,+], Shuting Li[b,+], Xiao Ou[b], Jungyoun Cho[a], Ao Li[b], Gerhard Hofer[a], Jiaoyan Xu[a], Taimin Yang[a], Xiaodong Zou[a], Ming Lu[*b], Hongyi Xu[*a]

[a]Department of Materials and Environmental Chemistry, Stockholm University, Stockholm SE-106 91, Sweden.
E-mail: hongyi.xu@mmk.su.se

[b]School of Pharmaceutical Sciences, Sun Yat-sen University, Guangzhou 510275, China.
E-mail: luming3@mail.sysu.edu.cn

[+]There authors contributed equally.

Abstract

3D electron diffraction (3D ED), also known as MicroED, has shown great potential in crystal structure determination in materials, small organic molecules, and macromolecules. In this work, a high-throughput 3D ED method has been implemented to identify six phases in an active pharmaceutical ingredient, griseofulvin (GSF). Batch data collection under low-dose conditions using the widely available commercial software EPU-D (Thermo Fisher Scientific) was combined with semi-automated data processing and clustering to collect and process over 100 datasets over three days. Accurate unit cell parameters obtained from 3D ED data allowed identification of GSF Forms III, I, GSF-and PEG IC-I, as well as three additional phases undetected in powder X-ray diffraction data, namely GSF II, GSF-V and a new phase GSF-PEG IC-II. Their structures were directly determined by 3D ED. Through structure analysis, we discovered polymorphism within inclusion complexes built from the same clinical drug-polymer combination. These results demonstrate the ability of the high-throughput method to accurately reveal the phase information of complex, beam-sensitive crystallisation products, which is significant for drug design where crystal form screening is crucial for the overall efficacy of the drug product.

Introduction

Structural knowledge of the active pharmaceutical ingredient (API) solid form is extremely important in drug development. Conventional API solid forms include polymorphs of the pure drug molecule, its salts, solvates/hydrates and co-crystals between the drug molecule and other pharmaceutically accepted co-formers. Due to differences in lattice interactions, the solid forms adopted by an API can exhibit large differences in their stability, solubility and dissolution properties, and ultimately, the overall bioavailability of the API. Therefore, the physicochemical properties of solid formulated drugs can be tailored by specific solid form selection and identifying and characterising the available solid forms of an API is critical for selecting, or even engineering, the optimal solid form. Preparing and characterising a large proportion of the available solid forms of an API can be a challenging process that often requires a sound screening strategy with intelligent and high-throughput experimentation[1–4].

Single-crystal X-ray crystallography (SCXRD) provides detailed structural information from the solid state. Although the vast majority of small molecule crystal structures are determined by SCXRD, the technique is limited by crystal size and quality requirements, and as a result, SCXRD is unfeasible for phase analysis. Instead, powder X-ray diffraction (PXRD) is commonly used during various stages of solid form screening to identify and characterise new forms. However, peak overlapping resulting from the three-dimensional diffraction data being compressed into one dimension can limit phase identification, especially when the sample contains phases with similar unit cell parameters, large unit cell parameters or low symmetry space groups[5]. Additionally, minor phases present in very low amounts may not be detected. Therefore, some solid forms may be left undiscovered when using PXRD as the primary phase analysis tool during screening.

3D electron diffraction (3D ED), also known as MicroED, is a crystallographic technique capable of structure determination from micrometre-sized crystals and has been used to determine a number of small molecule crystal structures[6–26]. Two studies from 2018 highlighted the potential of 3D ED (also known as MicroED) as a phase analysis tool for the pharmaceutical industry by rapid structure determination and solving numerous small molecule structures from an artificial heterogeneous mixture[10,11]. When collecting 3D ED data, single crystals can be selected from multiphasic mixtures, allowing the crystal structures of individual phases to be determined. Since structure determination can be achieved from just one crystal, phases in nanomolar amounts can also be detected and characterised. Yet, most 3D ED data collection is performed manually and is a time-consuming process. Generally, only a few

datasets (10 to 20) are collected over a half-day session, even though there are usually thousands of crystals on the grid, meaning typical sample sizes are inadequate in describing the bulk material for phase analysis and minor phases may go undetected.

Several automated 3D ED data collection procedures have been developed to reduce the operating time of the user and increase throughput[27–30]. Serial electron diffraction (SerialED), involving the acquisition of a single frame from each crystal, has been developed with crystal mapping in low-mag imaging[27] and scanning transmission electron microscopy (STEM)[30] modes. Although these methods lower dose accumulation, increase resolution and are fully automated, identifying phases from multiphasic systems with similar unit cell parameters from single frames can be challenging. Building on SerialED, serial rotation electron diffraction (SerialRED) has been developed as a fully automated technique for three-dimensional data collection[29] and applied for the phase identification of multiphasic zeolite[31] and metal-organic framework mixtures[29]. Recently, by automatically and rapidly examining hundreds of crystals, SerialRED enables high-throughput phase analysis and allows the exploration of complex synthesis systems[32]. However, the rotation ranges of each dataset are often low in the current implementation due to the alignment of the goniometer and relative high electron dose rate used in the current SerialRED implementation[32]. This can lead to reduced accuracy in unit cell parameters, which can hinder phase identification from multiphasic systems with similar unit cells. In addition, structure determination of any new phases often requires merging datasets collected on multiple crystals, limiting the method's sensitivity to detect and characterise minor phases.

Rapid and accurate phase analysis of pharmaceuticals is of great importance. In order to apply SerialRED to more beam-sensitive pharmaceuticals crystals, cryo-EM and low dose 3D ED data collection protocol, similar to those used for study protein crystals by MicroED[33–35] were applied. Furthermore, we combined the widely available commercial software EPU-D (Thermo Fisher Scientific) for batch data collection with the program *edtools* for semi-automated data processing and clustering[29]. When collecting data in batch mode, crystal locations are manually selected and added to a list. Tilt-series are then automatically collected from all positions on the list with a constant rotation range. The mechanical eucentric height near each pre-defined crystal position was automatically aligned before 3D ED data collection, to improve overall tilt range. Using this method, hundreds of datasets with large rotation ranges, typically greater than 80 degrees, can be collected and processed in only a few days. Furthermore, the accumulated electron dose of each dataset was less than 1 $e^-/Å^2$ (~3.8 MGy).

Here, we demonstrate the application of the high-throughput method in the phase analysis of a polycrystalline product resulting from the melt crystallisation of a griseofulvin (GSF) and polyethylene (PEG) mixture. GSF is an orally-administered antifungal drug and has five polymorphic forms (**Table S1**)[36–40]. Since the drug is poorly water-soluble, GSF has been formulated as an inclusion complex (IC) with PEG (GSF-PEG IC) to improve the dissolution behaviour[41,42]. During previous studies on the melt crystallisation of GSF from dispersions with PEG[40], we discovered a spherulite nucleating at 80 °C in 90% GSF-10% PEG 1000. The spherulite had a unique melting behaviour (transforming completely to GSF Form V once heated above 120 °C) and showed a small shift in the Raman spectrum at 1660 cm^{-1} (**Figures S1** and **S2**). These properties indicated the discovery of a new crystal form.

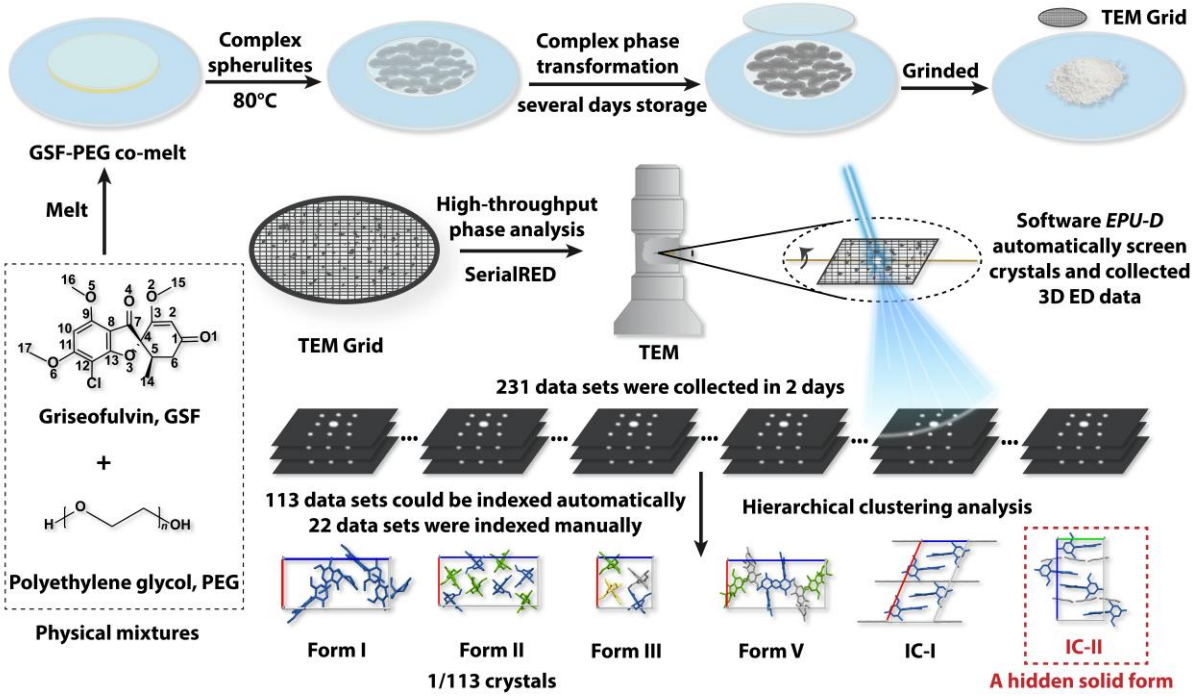

Figure 1. High-throughput 3D ED reveals a hidden phase from a six-phase sample

The new crystal form was however not stable. By PXRD data collected over 10 days, we found that a series of phase transformation events had occurred. The final phase-stable spherulite is a mixture of the new GSF crystal form and a few other GSF polymorphs, as some peaks in the PXRD pattern (at 10, 15 and 23 2θ, in particular) related strongly to peaks of GSF Form I (**Figure 2 and S3**). To gain a more accurate understanding of the phases present in the GSF/PEG melt crystallisation product, we applied the high-throughput 3D ED method.

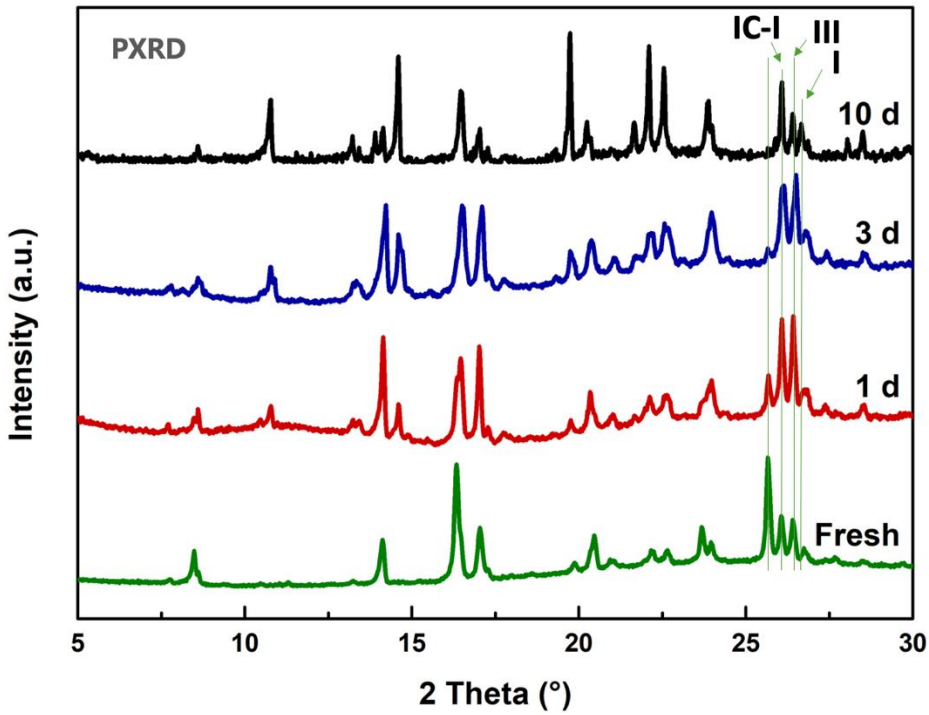

Figure 2. PXRD pattern collected directly after the synthesis of GSF/PEG spherulites and PXRD patterns collected from the same batch of sample after storage at ambient condition for 1, 3 and 10 days, respectively.

Results

Phase identification

The phase-stable spherulite stored for several days including shipping (from China to Sweden) was analysed. To perform a low dose high-throughput phase analysis, we used a method that combined the commercial software EPU-D (Thermo Fisher Scientific) installed on a cryo-TEM for data collection in batch mode with the program *edtools* for semi-automated data processing and clustering[43]. An atlas of the grid was collected, and suitable crystals were selected manually for data collection. The eucentric height was corrected for each crystal, to maximize the rotation range, which was stored along with the grid locations in the batch list. Tilt-series (-40° to +40°) were then automatically collected from the pre-selected locations in the batch list. For data processing, we utilised the workflow implemented in *edtools* (**Figure S4**), which adopts a hierarchical clustering analysis (HCA) algorithm to group datasets belonging to the same phase based on the Euclidean distance of the unit cell parameters (**Eq. S1**), as well as the correlation coefficients (CC) between intensities of common reflections in different datasets.

Using this method, 231 datasets were collected in two full-day 3D ED sessions. 113 of these datasets could be indexed using *edtools* without any supervision. Five phases were revealed by the HCA alongside three outlying datasets (**Figure 3**). Based on the automated high-throughput data analyses, it was found that the major phases in the sample were GSF Form III (45 datasets, cluster 2) and GSF Form I (31 datasets, cluster 4). Crystals of GSF-PEG IC (15 datasets, cluster 1) and the new solid form (12 datasets, cluster 3) were also found. The smallest cluster (7 datasets, cluster 5) consisted of crystals of GSF Form V, and one outlying dataset was collected from a GSF Form II crystal. One of the remaining unclassified datasets was collected from an ice crystal and the other from an agglomerate. Overall, the clustering analysis revealed six phases in the melt crystallisation product, GSF Forms I, II, III and V, GSF-PEG IC and the new solid form. The unit cell parameters of all datasets are reported in **Table S2**. Out of the 118 datasets that could not be indexed initially, 22 could be indexed after XDS was re-run with manually inputted unit cell parameters of one of the six phases found (**Table S3**). The remaining 95 datasets either showed too weak diffraction spots, no diffraction at all or were agglomerates. It is worth mentioning that although this seems like a large proportion, specific crystal morphologies were not targeted and crystals were not tested for diffraction before being added to the batch list. Instead, poorly diffracting crystals were eliminated during processing to increase the efficiency of the data collection set-up and minimize bias in crystal picking.

The findings of the clustering analysis are substantiated by the Pawley fit of the PXRD pattern collected from the spherulite using the six phases found (**Figure S5**). The PXRD pattern can be well fitted with the major phases, GSF Forms I and III and GSF-PEG IC1. No obvious peaks from the new crystal form or GSF Forms II and V were observed, and the Pawley fit was not significantly improved by including them.

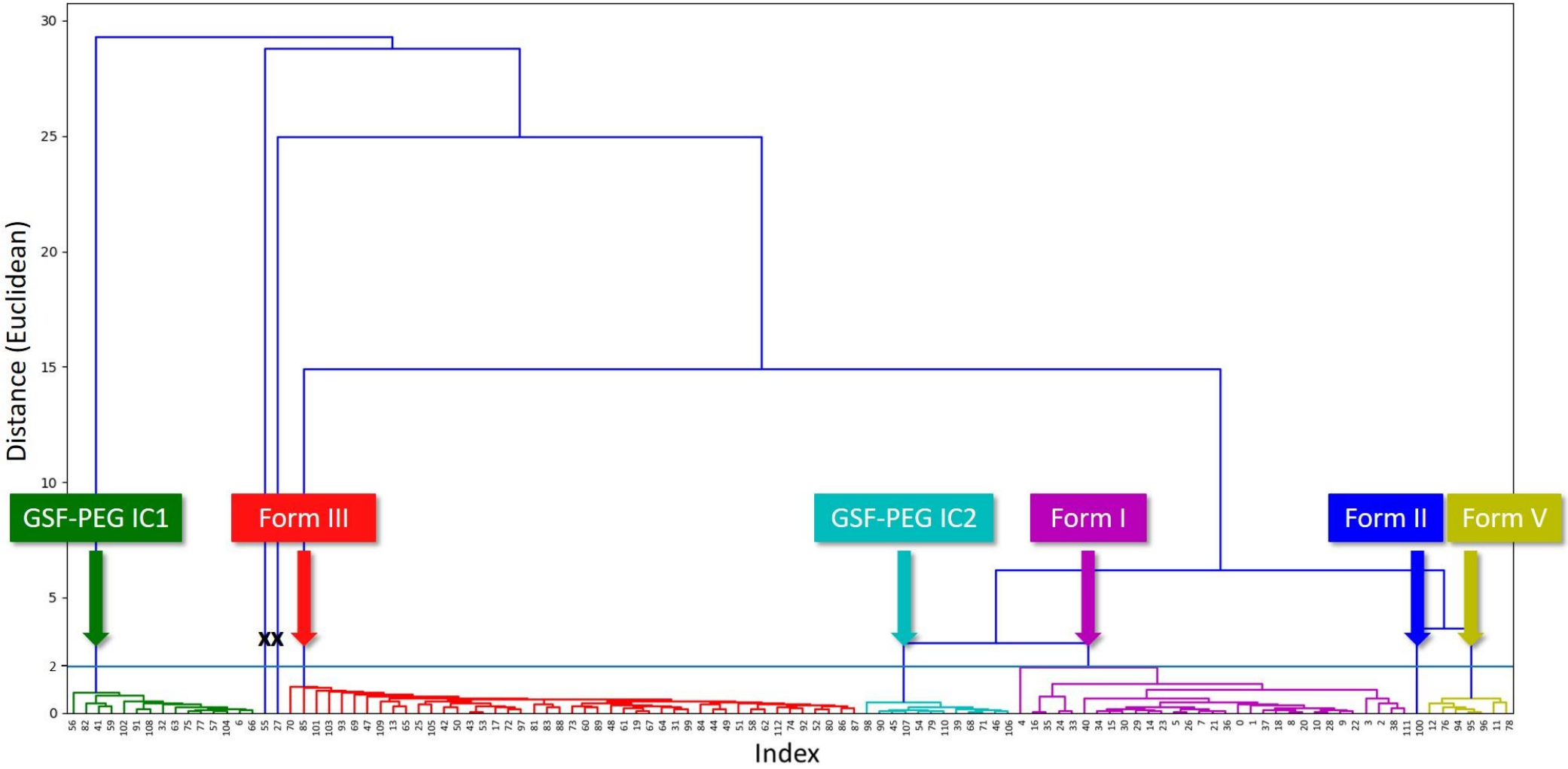

Figure 3. Dendrogram showing the results of the hierarchical clustering analysis (HCA) of the 113 indexed datasets. Clustering based on the Euclidean distance between the unit cell parameters using a threshold of 2.0 revealed six phases in the polycrystalline GSF/PEG melt crystallisation product. The major phases were GSF Form I and Form III. Two inclusion complexes (ICs) of GSF and PEG were also present together with GSF Forms V and II. One of the unclassified datasets was collected from an ice crystal and the other from an agglomerate. The unit cell parameters of all datasets are reported in Table S2.

Structure determination

After identifying the phases present in the melt crystallisation product, the crystal structure of each phase was solved following the workflow implemented in *edtools.* Only the datasets that could be indexed without inputting unit cell parameters were merged for structure solution to demonstrate the autonomous capability of the method. The datasets in each cluster were scaled and merged, and a second stage HCA based on correlation coefficient values (**Eq. S2**), which characterise the correlation of intensities of common reflections between datasets, was then run. After a cut-off of 0.3 (corresponding to CC=91) was chosen (**Figure S6**), a merged hkl file of the selected datasets was created for structure solution. The crystal structure of each phase was solved *ab initio* using SIR2014[44] and refined using SHELXL[45,46]. The crystallographic and refinement data are reported in **Table S4**.

The crystal structures of the five polymorphic forms[36–40] and GSF-PEG IC-I[47] have been determined previously. The resulting crystal structures of GSF-PEG IC-I and GSF Forms I, II, III and V (**Figure S7)** are highly consistent with the previously reported structures solved by SCXRD with minimal root-mean-square deviations (RMSDs) (**Table S5**).

Previous structural characterisation of GSF-PEG IC-I was carried out using SCXRD, PXRD and solid-state nuclear magnetic resonance spectroscopy[41,42,47]. The GSF-PEG IC-I crystal structure was obtained in the monoclinic space group $C2$ with unit cell parameters a = 21.89 (31) Å, b = 8.67 (12) Å, c = 11.70 (34) Å, α = 90 °, β = 113.38 (17) °, γ = 90 ° (**Table S4**). These parameters are similar to the previous data determined by SCXRD[47] and PXRD[41]. Indeed GSF-PEG IC is isostructural with the GSF-nitroethane solvate[48]. The channels of GSF molecules, extending along the crystallographic *c*-axis, interact via C-H···O and Cl···O interactions (**Figures 4** and **S8**), as described previously[47,48]. Positive density in the difference potential map between the GSF channels indicated the presence of the disordered PEG molecules.

A structure model of the new solid form was obtained in the orthorhombic space group $P2_12_12_1$ with unit cell parameters a = 20.33 (16) Å, b = 8.61 (5) Å, c = 11.76 (6) Å, α = 90 °, β = 90 °, γ = 90 ° (**Table S4**). The crystal structure revealed that the form is also an IC of GSF and PEG, with GSF channels extending along the crystallographic *c*-axis that are isostructural with the GSF nitromethane solvate[48]. The presence of the disordered PEG molecules could again be confirmed by the positive density in the difference potential map. The difference in packing of the two ICs arises from the conformational differences of the GSF

molecules stemming from the free rotation of the cyclohexanone ring with respect to the benzofuran ring moiety and has been well documented previously in the study of GSF solvates[48]. To the best of our knowledge, this is the first time polymorphism has been observed within ICs built from the same combination of clinical drug and polymer. We propose to name the first reported IC as GSF-PEG IC1 and the novel IC discovered in this work as GSF-PEG IC2.

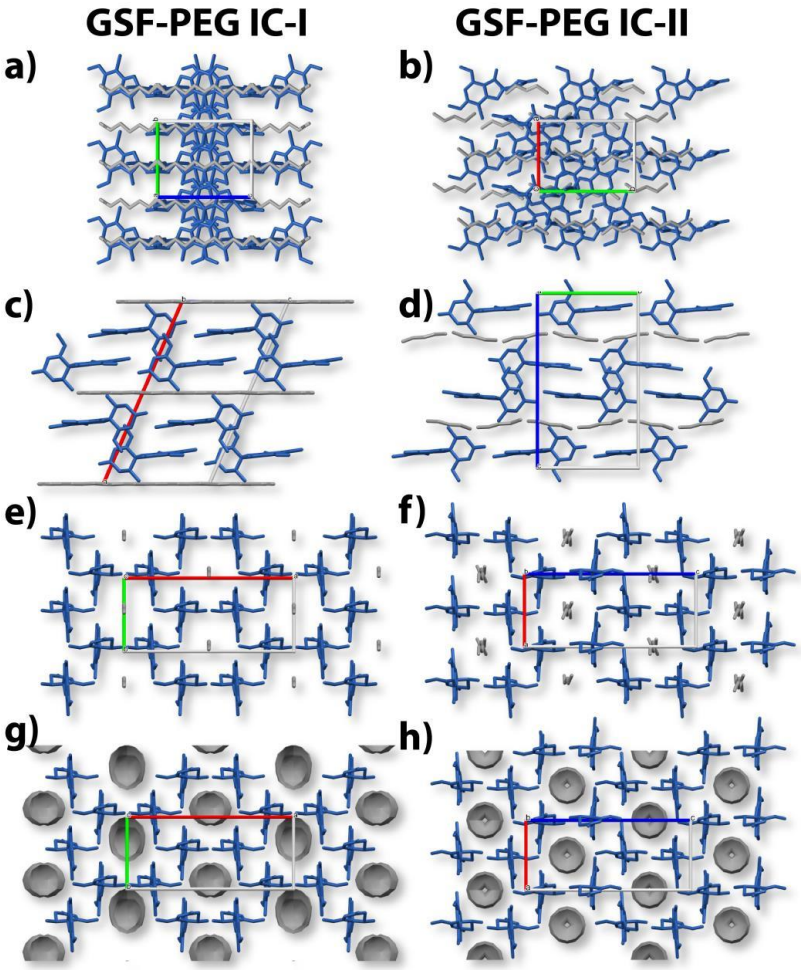

Figure 4. Crystal structures (a-f) and channel frameworks (g-h) of GSF-PEG IC-I and GSF-PEG IC-II.

Discussion

Collecting 3D ED data manually is a time-consuming process, while sample sizes are often too small to represent the bulk sample, and minor phases may go undetected. High-throughput collection allows data to be collected on several hundreds of crystals per day, allowing phase analysis and structure determination of new crystal phases directly. In traditional 3D ED data

collection, the user tends to pick crystals of well-defined morphology for data collection, because these are mostly likely to diffract well. High throughput data collection protocol provided the opportunity to minimize bias in crystal picking. Furthermore, by collecting data in batch mode, the operating time of the user is much shorter. The actual 3D ED data collection is automated and can run for several hours without supervision.

By combining the cryo-EM and low dose data collection protocols implemented in EPU-D, the accumulated electron dose for each 3D ED dataset was below 1 e-/Å^2 in a 300kV electron microscope, which is approximately 3.8 MGy per crystal. No visible evidence of beam damage was observed in the reconstructed 3D reciprocal lattice. The protocol reported in this work is applicable to most organic small molecule crystals and macromolecule crystals.

The GSF polymorphs and ICs with PEG have similar unit cell parameters, which, along with their presence in varying amounts, made the minor phases in the melt crystallisation product impossible to be identified by PXRD. High quality 3D ED data was collected for accurate unit cell determination in order to identify the six phases in the polycrystalline GSF/PEG melt crystallisation product. This is well supported by the dendrogram showing the results of the clustering analysis based on unit cell parameters (**Figure 3**) and the small deviations of the unit cell parameters determined from individual crystals (**Table S2**). Furthermore, by calibrating the eucentric height for each crystal before data collection, 3D ED dataset could be collected over a large rotation range. The high completeness of individual dataset allowed directly structure determination of the six phases found in the spherulite. This is a significant improvement in high-throughput 3D ED/MicroED analysis.

As shown in **Figure S5**, all major peaks in the PXRD data collected from the spherulite could be fitted by only including 3 out of the 6 phases identified by high-throughput 3D ED, namely GSF Form III (45/113 crystals), GSF Form I (31/113 crystals), and GSF-PEG IC-I (15/113 crystals). The 2 minor phases, GSF-PEG IC-II (12/113 crystals) and GSF-V (7/113 crystals), found by 3D ED were 'invisible' in PXRD data. Furthermore, the identification of the very minor phase GSF-V (1/113 crystals) illustrates the great sensitivity of high-throughput 3D ED in phase analysis studies.

The original high-throughput 3D ED workflow, named SerialRED, was developed on an open source python based software *Instamtic*[27,32,43]. The software is versatile and has been used as a platform for electron crystallography method development. However, expertise and experiences are needed to install and configure the software on different microscope/detector

setups. Similar automated data collection software, such as Leginon[49] for MicroED and SerialEM based scripts[50,51] have also been developed by research groups around the world. Commercialized software packages such as EPU-D by ThermoFisher Scientific, Latitude-D by GATAN, and CrysAlis^{Pro} for ED by JEOL-Rigaku offer an alternative for 3D ED/MicroED data collection on widely available TEMs, cryo-TEMs, and dedicated electron diffractometers. Although they are not yet optimized for fully automated data collection, using the batch collection function and manual crystal picking, high-throughput phase analysis could be performed as shown in this work. All these developments significantly improve the availability of 3D ED/MicroED.

The next phase of the development is to implement a robust crystal picking algorithm for fully automated 3D ED data collection and analysis[32]. The current crystal picking function implemented in *Instamatic* is based on analysing the contrast in micrographs. In order for the algorithm to work, continuous carbon supporting film is necessary. Recent development in artificial intelligence, like those implemented for particle picking in single particle analysis[52–54], provides new opportunities for more robust crystal picking. It will further improve the throughput of 3D ED data collection, completely remove bias in crystal picking and enable unsupervised phase analysis.

By identifying and characterising the six phases present in the GSF/PEG melt crystallisation product, the first case of polymorphism within ICs built from the same clinical drug-polymer combination could be observed. The discovery of the new IC demonstrates that drug molecules that form more than one channel solvate can form more than one IC with the same linear polymer, and these ICs may exhibit large differences in stability. The stability of ICs has previously been altered by changing the type[55] or molecular weight[56,57] of the guest polymer. This strategy can now be combined with searching for drug molecules that form more than one channel solvate as an additional approach to engineering an IC with optimal physicochemical properties.

Conclusions

A phase analysis of a polycrystalline melt crystallisation product was performed using a high-throughput method that combines 3D ED data collection using the commercial software EPU-D from Thermo Fischer Scientific in batch mode with the program *edtools* for semi-automated data processing and clustering. Over 100 high-quality 3D ED datasets with a consistent rotation

range of -40 ° to +40 ° were collected and processed over three days. Benefiting from the accurate unit cell parameter determination, six phases present in varying amounts were identified by hierarchical clustering using the Euclidean distance as the selection criteria. The crystal structure of each phase was obtained, including the two novel crystal structures of GSF-PEG IC-I and GSF-PEG IC-II. The minor phases detected, GSF Forms V and II and GSF-PEG IC-II, were present in too small amounts to be detected by PXRD. The first case of polymorphism within ICs built from the same clinical drug-polymer combination was reported, and the possibility of tuning the stability of an IC \by selecting drugs that form multiple channel solvates was suggested. These results demonstrate the selectivity and sensitivity of the high-throughput method to accurately reveal the phase information of complex crystallisation products, which is significant for drug design where screening for and selecting the optimal crystal form is crucial for the overall efficacy of the drug product.

Acknowledgement

We acknowledge funding from the Swedish Research Council (2017-05333, 2019-00815), the Knut and Alice Wallenberg Foundation (2019.0124), and the SciLifeLab technology development project (MicroED@SciLifeLab). We thank the Guangdong Basic and Applied Basic Research Foundation (No. 2020A1515010782 and 2022A1515010393).

References

1 C. R. Gardner, C. T. Walsh and Ö. Almarsson, *Nat Rev Drug Discov*, 2004, **3**, 926–934.
2 M. von Raumer and R. Hilfiker, in *Polymorphism in the Pharmaceutical Industry*, John Wiley & Sons, Ltd, 2018, pp. 1–30.
3 R. Hilfiker, F. Blatter, M. Szelagiewicz and M. von Raumer, in *Polymorphism in the Pharmaceutical Industry*, John Wiley & Sons, Ltd, 2018, pp. 241–259.
4 A. J. Cruz-Cabeza, S. M. Reutzel-Edens and J. Bernstein, *Chem. Soc. Rev.*, 2015, **44**, 8619–8635.
5 R. A. Storey, I. Ymén and I. Ymén, *Solid State Characterization of Pharmaceuticals*, John Wiley & Sons, Incorporated, Hoboken, UNITED KINGDOM, 2011.
6 M. Gemmi, M. G. I. La Placa, A. S. Galanis, E. F. Rauch and S. Nicolopoulos, *J Appl Cryst*, 2015, **48**, 718–727.
7 E. van Genderen, M. T. B. Clabbers, P. P. Das, A. Stewart, I. Nederlof, K. C. Barentsen, Q. Portillo, N. S. Pannu, S. Nicolopoulos, T. Gruene and J. P. Abrahams, *Acta Crystallogr A Found Adv*, 2016, **72**, 236–242.
8 Y. Wang, S. Takki, O. Cheung, H. Xu, W. Wan, L. Öhrström and A. K. Inge, *Chem. Commun.*, 2017, **53**, 7018–7021.

9 P. P. Das, E. Mugnaioli, S. Nicolopoulos, C. Tossi, M. Gemmi, A. Galanis, G. Borodi and M. M. Pop, *Org. Process Res. Dev.*, 2018, **22**, 1365–1372.
10 T. Gruene, J. T. C. Wennmacher, C. Zaubitzer, J. J. Holstein, J. Heidler, A. Fecteau-Lefebvre, S. De Carlo, E. Müller, K. N. Goldie, I. Regeni, T. Li, G. Santiso-Quinones, G. Steinfeld, S. Handschin, E. van Genderen, J. A. van Bokhoven, G. H. Clever and R. Pantelic, *Angew Chem Int Ed Engl*, 2018, **57**, 16313–16317.
11 C. G. Jones, M. W. Martynowycz, J. Hattne, T. J. Fulton, B. M. Stoltz, J. A. Rodriguez, H. M. Nelson and T. Gonen, *ACS Cent Sci*, 2018, **4**, 1587–1592.
12 I. Andrusenko, V. Hamilton, E. Mugnaioli, A. Lanza, C. Hall, J. Potticary, S. R. Hall and M. Gemmi, *Angewandte Chemie International Edition*, 2019, **58**, 10919–10922.
13 P. Brázda, L. Palatinus and M. Babor, *Science*, 2019, **364**, 667–669.
14 C. G. Jones, M. Asay, L. J. Kim, J. F. Kleinsasser, A. Saha, T. J. Fulton, K. R. Berkley, D. Cascio, A. G. Malyutin, M. P. Conley, B. M. Stoltz, V. Lavallo, J. A. Rodríguez and H. M. Nelson, *ACS Cent. Sci.*, 2019, **5**, 1507–1513.
15 I. Andrusenko, J. Potticary, S. R. Hall and M. Gemmi, *Acta Crystallogr B Struct Sci Cryst Eng Mater*, 2020, **76**, 1036–1044.
16 B. J. Curtis, L. J. Kim, C. J. J. Wrobel, J. M. Eagan, R. A. Smith, J. E. Burch, H. H. Le, A. B. Artyukhin, H. M. Nelson and F. C. Schroeder, *Org. Lett.*, 2020, **22**, 6724–6728.
17 P. P. Das, A. G. Pérez, A. S. Galanis and S. Nicolopoulos, *Microscopy and Microanalysis*, 2020, **26**, 1522–1522.
18 G. R. Woollam, P. P. Das, E. Mugnaioli, I. Andrusenko, A. S. Galanis, J. van de Streek, S. Nicolopoulos, M. Gemmi and T. Wagner, *CrystEngComm*, 2020, **22**, 7490–7499.
19 M. Lightowler, S. Li, X. Ou, X. Zou, M. Lu and H. Xu, *Angewandte Chemie International Edition*, 2022, **61**, e202114985.
20 I. Andrusenko, V. Hamilton, A. E. Lanza, C. L. Hall, E. Mugnaioli, J. Potticary, A. Buanz, S. Gaisford, A. M. Piras, Y. Zambito, S. R. Hall and M. Gemmi, *International Journal of Pharmaceutics*, 2021, **608**, 121067.
21 L. J. Kim, M. Xue, X. Li, Z. Xu, E. Paulson, B. Mercado, H. M. Nelson and S. B. Herzon, *J. Am. Chem. Soc.*, 2021, **143**, 6578–6585.
22 T. Yang, S. Waitschat, A. K. Inge, N. Stock, X. Zou and H. Xu, *Symmetry*, 2021, **13**, 2131.
23 E. T. Broadhurst, H. Xu, S. Parsons and F. Nudelman, *IUCrJ*, 2021, **8**, 860–866.
24 E. T. Broadhurst, H. Xu, M. T. B. Clabbers, M. Lightowler, F. Nudelman, X. Zou and S. Parsons, *IUCrJ*, 2020, **7**, 5–9.
25 J. F. Bruhn, G. Scapin, A. Cheng, B. Q. Mercado, D. G. Waterman, T. Ganesh, S. Dallakyan, B. N. Read, T. Nieusma, K. W. Lucier, M. L. Mayer, N. J. Chiang, N. Poweleit, P. T. McGilvray, T. S. Wilson, M. Mashore, C. Hennessy, S. Thomson, B. Wang, C. S. Potter and B. Carragher, *Frontiers in Molecular Biosciences*, 2021, **8**, 354.
26 J. Burch, A. G. Smith, S. Caille, S. D. Walker, R. Wurz, V. J. Cee, J. Rodriguez, D. Gostovic, K. Quasdorf and H. M. Nelson, *ChemRxiv*, , DOI:10.33774/chemrxiv-2021-h3tqz.
27 S. Smeets, X. Zou and W. Wan, *J Appl Crystallogr*, 2018, **51**, 1262–1273.
28 M. J. de la Cruz, M. W. Martynowycz, J. Hattne and T. Gonen, *Ultramicroscopy*, 2019, **201**, 77–80.
29 B. Wang, X. Zou and S. Smeets, *IUCrJ*, 2019, **6**, 854–867.
30 R. Bücker, P. Hogan-Lamarre, P. Mehrabi, E. C. Schulz, L. A. Bultema, Y. Gevorkov, W. Brehm, O. Yefanov, D. Oberthür, G. H. Kassier and R. J. Dwayne Miller, *Nat Commun*, 2020, **11**, 996.
31 Y. Luo, B. Wang, S. Smeets, J. Sun, W. Yang and X. Zou, , DOI:10.26434/chemrxiv-2021-34v44.
32 Y. Luo, B. Wang, S. Smeets, J. Sun, W. Yang and X. Zou, *Nat. Chem.*, 2023, **15**, 483–490.

33 B. L. Nannenga, D. Shi, A. G. W. Leslie and T. Gonen, *Nat Methods*, 2014, **11**, 927–930.
34 H. Xu, H. Lebrette, M. T. B. Clabbers, J. Zhao, J. J. Griese, X. Zou and M. Högbom, *Sci. Adv.*, 2019, **5**, eaax4621.
35 M. T. B. Clabbers, S. Holmes, T. W. Muusse, P. R. Vajjhala, S. J. Thygesen, A. K. Malde, D. J. B. Hunter, T. I. Croll, L. Flueckiger, J. D. Nanson, Md. H. Rahaman, A. Aquila, M. S. Hunter, M. Liang, C. H. Yoon, J. Zhao, N. A. Zatsepin, B. Abbey, E. Sierecki, Y. Gambin, K. J. Stacey, C. Darmanin, B. Kobe, H. Xu and T. Ve, *Nat Commun*, 2021, **12**, 2578.
36 G. Malmros, A. Waägner and L. Maron, *Cryst. Struct. Commun.*, 1977, **6**, 463–470.
37 A. Mahieu, J. Willart, E. Dudognon, M. D. Eddleston, W. Jones, F. Danède and M. Descamps, *Journal of Pharmaceutical Sciences*, 2013, **102**, 462–468.
38 Y. Su, J. Xu, Q. Shi, L. Yu and T. Cai, *Chem. Commun.*, 2018, **54**, 358–361.
39 X. Ou, X. Li, H. Rong, L. Yu and M. Lu, *Chem. Commun.*, 2020, **56**, 9950–9953.
40 X. Ou, S. Li, Y. Chen, H. Rong, A. Li and M. Lu, *Crystal Growth & Design*, , DOI:10.1021/acs.cgd.2c00156.
41 Z. Zhong, C. Guo, L. Chen, J. Xu and Y. Huang, *Chem. Commun.*, 2014, **50**, 6375–6378.
42 X. Yang, Z. Zhong and Y. Huang, *International Journal of Pharmaceutics*, 2016, **508**, 51–60.
43 B. Wang, X. Zou and S. Smeets, *IUCrJ*, 2019, **6**, 854–867.
44 M. C. Burla, R. Caliandro, B. Carrozzini, G. L. Cascarano, C. Cuocci, C. Giacovazzo, M. Mallamo, A. Mazzone and G. Polidori, *J Appl Cryst*, 2015, **48**, 306–309.
45 G. M. Sheldrick, *Acta Cryst C*, 2015, **71**, 3–8.
46 C. B. Hübschle, G. M. Sheldrick and B. Dittrich, *J Appl Cryst*, 2011, **44**, 1281–1284.
47 X. Ou, S. Li, Y. Chen, H. Rong, A. Li and M. Lu, *Polymorphism in Griseofulvin: New Story of an Old Drug with Polyethylene Glycol*, Chemistry, 2021.
48 S. Aitipamula, P. S. Chow and R. B. H. Tan, *Acta Crystallogr B Struct Sci Cryst Eng Mater*, 2014, **70**, 54–62.
49 A. Cheng, C. Negro, J. F. Bruhn, W. J. Rice, S. Dallakyan, E. T. Eng, D. G. Waterman, C. S. Potter and B. Carragher, *Protein Science*, 2021, **30**, 136–150.
50 M. J. de la Cruz, M. W. Martynowycz, J. Hattne and T. Gonen, *Ultramicroscopy*, 2019, **201**, 77–80.
51 T. Sasaki, T. Nakane, A. Kawamoto, T. Nishizawa and G. Kurisu, *CrystEngComm*, 2023, **25**, 352–356.
52 C. O. S. Sorzano, R. Marabini, J. Velázquez-Muriel, J. R. Bilbao-Castro, S. H. W. Scheres, J. M. Carazo and A. Pascual-Montano, *Journal of Structural Biology*, 2004, **148**, 194–204.
53 F. Wang, H. Gong, G. Liu, M. Li, C. Yan, T. Xia, X. Li and J. Zeng, *Journal of Structural Biology*, 2016, **195**, 325–336.
54 T. Wagner, F. Merino, M. Stabrin, T. Moriya, C. Antoni, A. Apelbaum, P. Hagel, O. Sitsel, T. Raisch, D. Prumbaum, D. Quentin, D. Roderer, S. Tacke, B. Siebolds, E. Schubert, T. R. Shaikh, P. Lill, C. Gatsogiannis and S. Raunser, *Commun Biol*, 2019, **2**, 218.
55 L. Chen and Y. Huang, *RSC Adv.*, 2021, **11**, 13091–13096.
56 P. Chappa, A. Maruthapillai, R. Voguri, A. Dey, S. Ghosal and M. A. Basha, *Crystal Growth & Design*, 2018, **18**, 7590–7598.
57 X. Yang, Z. Zhong and Y. Huang, *International Journal of Pharmaceutics*, 2016, **508**, 51–60.